PHYSICAL REVIEW B **104**, 184519 (2021)

Theory for doping trends in titanium oxypnictide superconductors

Han-Xiang Xu,[1] Daniel Guterding,[2] and Harald O. Jeschke[1]
[1]*Research Institute for Interdisciplinary Science, Okayama University, Okayama 700-8530, Japan*
[2]*Fachbereich Mathematik, Naturwissenschaften und Datenverarbeitung, Technische Hochschule Mittelhessen, Wilhelm-Leuschner-Straße 13, 61169 Friedberg, Germany*

(Received 24 August 2021; revised 14 October 2021; accepted 19 November 2021; published 30 November 2021)

A family of titanium oxypnictide materials $\mathrm{BaTi_2}Pn_2\mathrm{O}$ (Pn = pnictogen) becomes superconducting when a charge and/or spin-density wave is suppressed. With hole doping, isovalent doping and pressure, a whole range of tuning parameters is available. We investigate how charge doping controls the superconducting transition temperature T_c. To this end, we use experimental crystal structure data to determine the electronic structure and Fermi surface evolution along the doping path. We show that a naive approach to calculating T_c via the density of states at the Fermi level and the McMillan formula systematically fails to yield the observed T_c variation. On the other hand, spin-fluctuation theory pairing calculations allow us to consistently explain the T_c increase with doping. All alkali-doped materials $\mathrm{Ba}_{1-x}A_x\mathrm{Ti_2Sb_2O}$ (A = Na, K, and Rb) are described by a sign-changing s-wave order parameter. Susceptibilities also reveal that the physics of the materials is controlled by a single Ti $3d$ orbital.

DOI: 10.1103/PhysRevB.104.184519

I. INTRODUCTION

The first layered titanium oxypnictides $Na_2Ti_2As_2O$ and $Na_2Ti_2Sb_2O$ were synthesized three decades ago [1] and discussed in terms of spin-density wave (SDW) or charge-density wave (CDW) behavior [2,3]. Nine years ago, superconductivity was discovered in $BaTi_2Sb_2O$ [4] and $BaTi_2Bi_2O$ [5]. By analysis of the $\mathrm{BaTi_2(As_{1-x}Sb_x)_2O}$ solid solutions it quickly became apparent that superconductivity is favored by a suppression of the CDW/SDW phase [6,7]. An extensive discussion of the phase transition observed in resistivity and magnetic susceptibility [2,4,8,9] as well as thermoelectric power and Hall coefficient [10] concerns the question whether it should be characterized as a CDW transition or if it is, in fact, a SDW transition. Experimental evidence from NMR [11] and muon spin relaxation (μSR) [12,13] does not completely resolve the question.

Shortly after the discovery of superconductivity, it was realized that both charge doping on the barium site and isovalent doping on the pnictogen site provide opportunities to control the superconductivity of $BaTi_2Sb_2O$ in a significant range. Hole doping via alkali metals increases T_c from 1.2 to 5.5 K in $\mathrm{Ba_{1-x}Na_xTi_2Sb_2O}$ [9,12], to 6.1 K in $\mathrm{Ba_{1-x}K_xTi_2Sb_2O}$ [14], to 5.4 K in $\mathrm{Ba_{1-x}Rb_xTi_2Sb_2O}$ [15], and to 4.4 K in $\mathrm{Ba_{1-x}Cs_xTi_2Sb_2O}$ [16]. The maximum T_c is reached near an alkali content of $x = 0.2$–0.3. Isovalent doping via Sb/Bi mixing yields an intriguing two-dome T_c evolution with a nonsuperconducting or low T_c phase in between [6,17]. More recently, pressure has been demonstrated to be an effective control parameter for superconductivity [18].

The nature of superconductivity in the titanium oxypnictides has been discussed since its discovery [19]. Experimentally, an s-wave gap has been inferred from nuclear quadrupole resonance (NQR) measurements [11], and specific heat is partially consistent with BCS expectations [20]. However, μSR measurements have been taken to indicate an unconventional pairing mechanism [21]. An NMR/NQR study points to significant differences in the superconductivity of $BaTi_2Sb_2O$ and $BaTi_2Bi_2O$ [22].

Theoretically, calculations of electron-phonon coupling have shown that the low transition temperature of $BaTi_2Sb_2O$ can be explained by an electron-phonon mechanism [23]. On the other hand, based on the Fermi surfaces a sign-changing s-wave state has been predicted within spin-fluctuation theory [24]. Although the presence of magnetism has not been fully established in the titanium oxypnictides, an extensive density functional theory (DFT) study and symmetry analysis of the nematicity and charge order in $BaTi_2Sb_2O$ have provided strong evidence that these materials cannot be understood without taking spin fluctuations into account [25].

Whereas the electronic structure of individual titanium oxypnictide metals [26,27] and superconductors [24,28,29] has been studied repeatedly, there is no theory for the evolution of properties with doping. Our study is intended to fill this gap. In this paper, we show that we can consistently explain the evolution of the superconducting T_c with alkali doping using spin-fluctuation theory and that the superconducting gap function has a sign-changing s-wave symmetry.

II. METHODS

We perform electronic structure calculations using the full potential local orbital (FPLO) basis set [30] and the generalized gradient approximation (GGA) to the exchange and correlation potential [31]. We use smooth interpolations of lattice parameters of the $P4/mmm$ space group (see Appendix A, Fig. 7) and optimize the antimony positions within the GGA. The charge doping is modeled via the virtual crystal approximation on the barium site. We use projective

Wannier functions as implemented in FPLO [32] to obtain 26 band tight-binding models including Ti $3d$ and $4s$, Ba $5d$, Sb $5p$, and O $2p$ orbital characters. The models follow DFT bands and Fermi surfaces to a high degree of accuracy (see Appendix B, Fig. 8). Based on the tight-binding model, we calculate noninteracting susceptibilities $\chi_{st}^{pq}(\mathbf{q})$. We apply the random-phase approximation (RPA) and investigate the pairing instabilities within spin-fluctuation theory by solving the gap equation on the Fermi surface [33–36] (for details, see Appendix D). Interaction parameters of $U = 2$ eV (intraorbital Coulomb repulsion), $U' = 1$ eV (interorbital Coulomb repulsion), $J = 0.5$ eV (Hund's rule coupling), and $J' = 0.5$ eV (pair hopping), applied to Ti $3d$ orbitals, were used for the RPA and pairing calculations. Note that a limitation of the RPA-based fluctuation theory is the restriction to zero energy, and application of the fluctuation exchange approximation (FLEX) which takes the energy dependence into account is an interesting future extension of our paper.

III. RESULTS

The titanium oxypnictide superconductors have been treated as simple BCS-type superconductors in various experimental [4,11,15,20,37] and theoretical [23] studies. As a straightforward attempt to understand the T_c tendencies, we extract the density of states at the Fermi level $N(E_F)$ as a function of doping and try to apply the BCS formula $T_c = 1.134\, T_D \exp(-\frac{1}{VN(E_F)})$ (with Debye temperature T_D and electron-phonon coupling potential V). Assuming constant T_D and V, this formula and its more sophisticated variants yield T_c trends that essentially follow $N(E_F)$. Note that our use of the virtual crystal approximation is justified by good comparison of our Fermi surfaces to angle-resolved photoemission (see Appendix C, Fig. 10). Nevertheless, conducting a similar study based on a more elaborate approach for treating alkali doping and Ba/alkali site disorder, such as the coherent potential approximation will be an interesting future endeavor.

Unfortunately, as Fig. 1 shows, there is very little similarity between $N(E_F)$ and T_c evolution with doping. In the case of alkali doping of $BaTi_2Sb_2O$, T_c quickly increases from $T_c = 1.2$ K to a maximum that is reached between doping levels of $x = 0.1$ to 0.3. Meanwhile, $N(E_F)$ remains constant until $x = 0.1$ before going through a minimum at $x = 0.23$ (Fig. 1). Based on this analysis, superconductivity in these materials could only be explained by an electron-phonon mechanism if the strength of electron-phonon coupling was extremely doping dependent so that it counteracts the unhelpful trends in $N(E_F)$. However, this seems very far fetched because in the small doping range considered, neither T_D nor V are expected to vary strongly. Therefore, we now turn to the possibility that the detailed evolution of the Fermi-surface nesting provides doping dependencies strong enough to explain the evolution of T_c within spin-fluctuation pairing theory. So far, the charge-density wave state has been studied with spin-fluctuation theory including Aslamazov-Larkin vertex corrections [38] or within dynamical mean-field theory [39] but only a limited study of superconductivity exists [28].

First, we identify the most relevant orbitals at the Fermi level. In Fig. 2(a), we show the band structure and density of states of $BaTi_2Sb_2O$ with Ti $3d$ and Sb $5p$ orbital characters highlighted. The system is, in general, quite strongly hybridized and many orbitals contribute to the states close to the Fermi level. Taking a closer look, we find that the most relevant Ti $3d$ orbital for the low-energy physics is $3d_{xy}$ followed by $3d_{xz,yz}$. To visualize the Ti $3d_{xy}$ orbital, we choose a local coordinate system for Ti where the z axis points along the Ti-O bond and x and y axes point along the Ti-Sb bonds. This is the natural local system to choose within the TiO_2Sb_4 octahedron [27] [Fig. 2(b)] since it makes $3d_{xz}$ and $3d_{yz}$ degenerate. Figure 2(c) shows the $3d_{xy}$ Wannier functions at both titanium sites (Ti1 and Ti2) based on this coordinate choice.

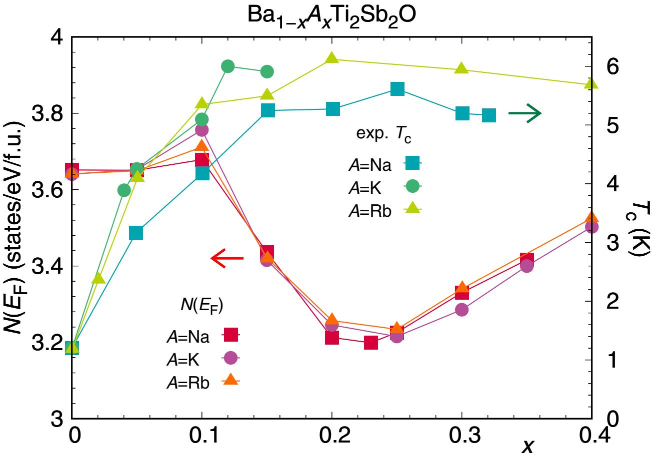

FIG. 1. Density of states at the Fermi level $N(E_F)$ shown together with experimental superconducting transition temperatures T_c for doping with three different alkali ions. T_c data are from Refs. [15,20] for Na doping, Ref. [14] for K doping, and Ref. [15] for Rb doping.

We now analyze the Fermi-surface evolution with alkali doping (Fig. 3). Only Ti $3d_{xy}$ and Sb $5p$ weights are highlighted (see Appendix C, Fig. 9 for the other $3d$ weights). Note that focusing on Ti and Sb is justified because relative contributions to the density of states at the Fermi-level $N(E_F)$ are 74%, 20%, 4%, and 1% for Ti, Sb, Ba, and O, respectively. The $BaTi_2Sb_2O$ Fermi surface is in excellent agreement with angle-resolved photoemission (ARPES) experiments [40,41] (see Appendix C, Fig. 10). We see that the hole Fermi surfaces at X and Y grow with doping whereas the electron Fermi surface at M shrinks slightly. The Fermi surface at Γ, which is dominated by Sb $5p$, shows a rather complicated reconstruction as a function of doping. This can be understood by tracing which orbital fillings are depleted by the holes introduced as a function of alkali-doping level x. In fact, the majority of doped holes are in Sb orbitals whereas Ti $3d$ orbitals are nearly unaffected. The changes seen in Fermi surfaces with Ti $3d$ character (Fig. 3) are due to stronger Sb-Ti bonding upon hole doping rather than due to a Fermi-level shift.

In order to measure the relative importance of the Fermi-surface changes, we turn to noninteracting susceptibilities calculated with the 26 band tight-binding models on $50 \times 50 \times 50$ integration meshes. Figure 4 shows that the total susceptibility χ_0 is clearly peaked at $\mathbf{q} = (\pi, 0, 0)$ (labeled X) and $\mathbf{q} = (0, \pi, 0)$ (labeled Y). Previously, this has been noted based on the Lindhard function calculated without matrix

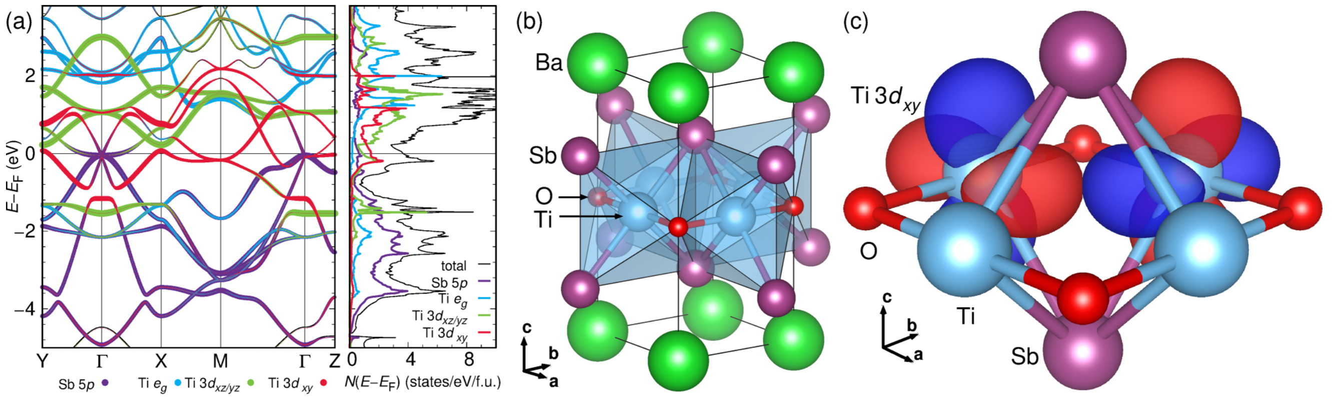

FIG. 2. (a) GGA band structure and density of states of $BaTi_2Sb_2O$. (b) Crystal structure of $BaTi_2Sb_2O$ with shaded TiO_2Sb_4 octahedra. (c) Ti $3d_{xy}$ Wannier functions within the Ti_2Sb_2O layer of $BaTi_2Sb_2O$.

elements [24,28]. With alkali doping, the peaks at X and Y decrease, and they also move away from the high-symmetry point towards Γ. At the same time, χ_0 at $\mathbf{q} = (0, 0, 0)$ decreases. Interestingly, the doping trends of the total χ_0 and χ_0^{xy} differ: Although the ratio between X and Γ values of χ_0 hardly changes with doping, this ratio sharply increases for χ_0^{xy} due to increases at X combined with decreases at Γ. This improved nesting is shown in Fig. 4(b) for Ti1 but equally applies to Ti2 where the Y to Γ ratio increases sharply. Furthermore, even though the Fermi surface shows substantial k_z dispersion, we can find the improved nesting also in the R to Z ratio. Meanwhile, the other orbitals, which are of some significance at the Fermi level ($3d_{xz}$ and $3d_{yz}$), have a comparatively featureless susceptibility [Fig. 4(c)] which uniformly decreases with doping. It is justified to focus on Ti $3d$ susceptibilities here because the Sb susceptibilities are small, almost flat with respect to $\mathbf{q}$ and they grow even more featureless with doping (see Fig. 11). Note that calculations without matrix elements, i.e., solely based on the Lindhard function, do not contain the orbital-resolved information we just discussed. Since alkali doping seems to lead to an overall decrease in susceptibility but strongly enhances the susceptibility of the Ti $3d_{xy}$ orbitals, we can expect them to be the main actor in T_c changes with doping.

Since the similarity of susceptibilities along the $k_z = 0$ and $k_z = \pi$ paths in Fig. 4(a) indicates a high degree of

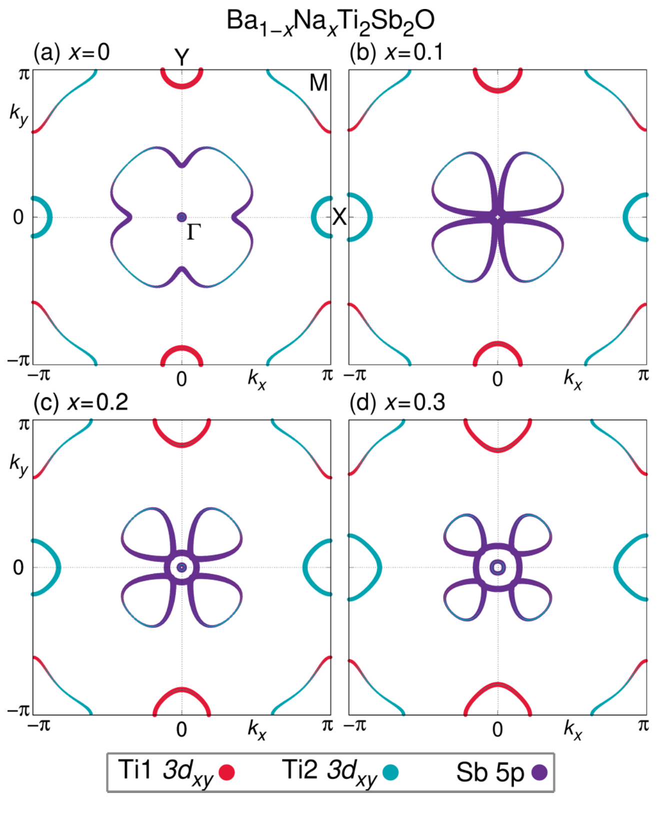

FIG. 3. Fermi surfaces of $Ba_{1-x}Na_xTi_2Sb_2O$ at $k_z = 0$ as function of doping level x, calculated within the GGA.

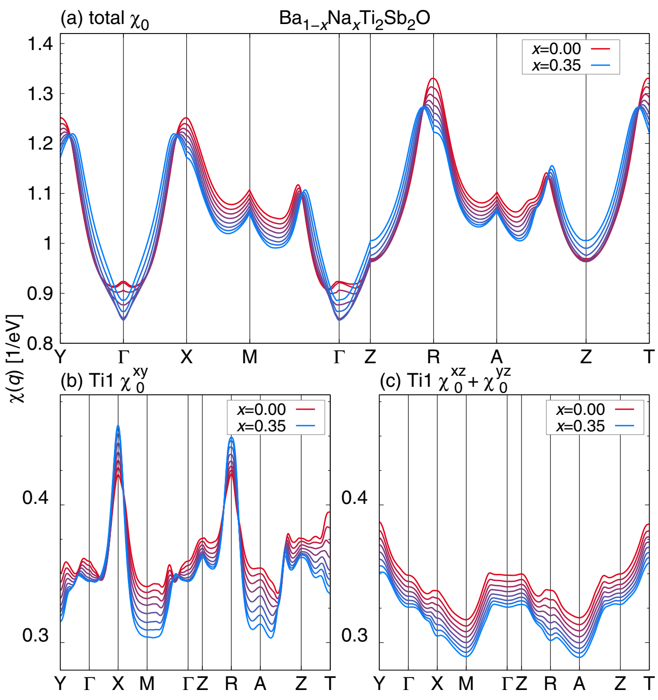

FIG. 4. Noninteracting susceptibility of $Ba_{1-x}Na_xTi_2Sb_2O$ for eight doping levels x. (a) Total, (b) $3d_{xy}$ contribution from Ti1, (c) $3d_{xz}$ and $3d_{xz}$ contributions from Ti1. $\mathbf{q} = (\pi, 0, 0)$ is labeled as X, $\mathbf{q} = (0, \pi, 0)$ as Y, $\mathbf{q} = (\pi, \pi, 0)$ as M, $\mathbf{q} = (0, 0, \pi)$ as Z, $\mathbf{q} = (0, \pi, \pi)$ as R, $\mathbf{q} = (\pi, \pi, \pi)$ as A and $\mathbf{q} = (\pi, 0, \pi)$ as T.

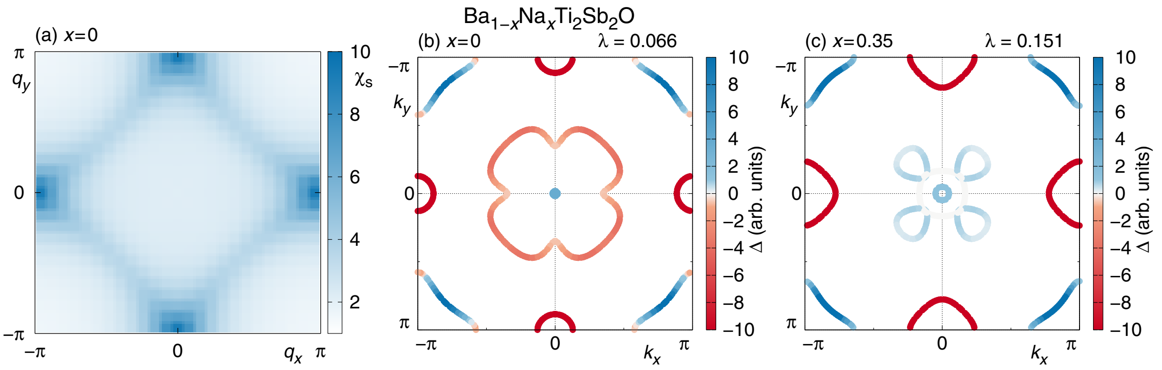

FIG. 5. Two-dimensional susceptibility and gap functions of Ba$_{1-x}$Na$_x$Ti$_2$Sb$_2$O. (a) Spin susceptibility χ_s calculated within the RPA for $x = 0$, showing enhanced maxima at $\mathbf{q} = (0, \pi)$ and $\mathbf{q} = (\pi, 0)$. (b) and (c) Eigenfunctions for the leading eigenvalue of the gap equation at zero doping and at maximal doping. The sign-changing s-wave persists at all doping levels.

two dimensionality, we now focus on the $k_z = 0$ cuts of susceptibility and pairing in Fig. 5. It is clear that features of the noninteracting susceptibility χ_0 (see Appendix E, Fig. 12), especially peaks at $\mathbf{q} = (\pi, 0)$ and $\mathbf{q} = (0, \pi)$, are enhanced in the interacting susceptibility obtained by random-phase approximation [Fig. 5(a)], reminiscent of single orbital system behavior. These instabilities would now favor stripe-type magnetism which, however, has not been observed for BaTi$_2$Sb$_2$O [11–13].

Here, the $(\pi, 0)$ and $(0, \pi)$ instabilities favor a sign-changing s-wave superconducting order parameter: The gap functions corresponding to the leading eigenvalue λ, obtained using spin-fluctuation theory, are shown in Figs. 5(b) and 5(c) for for two different doping levels. Subleading d_{xy}- and $d_{x^2-y^2}$-type solutions have far smaller eigenvalues and are, therefore, irrelevant in Ba$_{1-x}$Na$_x$Ti$_2$Sb$_2$O. The eigenvalue λ increases as a function of alkali doping (Fig. 6), and follows the doping trend of the maxima in the susceptibility [Fig. 4(a)]. Thus, the increase in T_c with alkali doping (Fig. 1) is clearly explained by the susceptibility trends rather than the density of states at the Fermi level. By performing the pairing calculations on three-dimensional (3D) Fermi surfaces, we have verified that the sign-changing s-wave is indeed the dominating solution for all alkali-doped materials Ba$_{1-x}A_x$Ti$_2$Sb$_2$O (A = Na, K, and Rb).

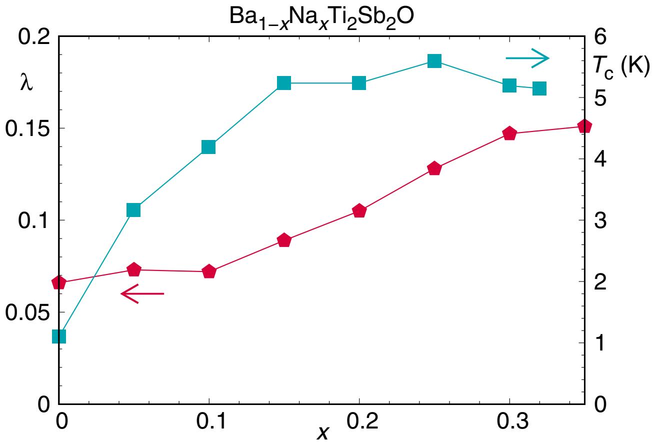

FIG. 6. Leading eigenvalues λ of the gap equation as a function of doping level x. T_c data are from Refs. [9,20].

At low alkali-doping levels we have found an order parameter, which contains nodes on the Fermi-surface sheets around M and a relatively large gap on the central Fermi-surface sheets around Γ. With increasing doping, the Fermi-surface sheets around M become nodeless, but the reconstructed sheets around Γ, which are almost exclusively of Sb 5p character, are hardly gapped at all. Those strongly nonuniform order parameters need to be taken into account when interpreting thermodynamic and other experiments trying to determine the symmetry of the superconducting state in titanium oxypnictides.

IV. CONCLUSIONS

We have investigated the electronic and superconducting properties of Ba$_{1-x}$Na$_x$Ti$_2$Sb$_2$O using density functional and spin-fluctuation theory. We modeled the crystal structure evolution using an interpolation of experimental lattice parameters and a DFT predicted antimony position. The density of states at the Fermi-level $N(E_F)$ shows a trend which is in sharp contrast to the evolution of the superconducting T_c, indicating that transition temperatures may not be accounted for by an electron-phonon mechanism.

Although the band structure and density of states show that constituents of Ba$_{1-x}A_x$Ti$_2$Sb$_2$O (A = Na, K, and Rb) are strongly hybridized and many orbitals lie close to the Fermi level, we have found that the susceptibility is completely dominated by the Ti 3d_{xy} orbitals.

Proceeding on the assumption of a magnetic pairing mechanism, which has been suggested by an investigation into the nematicity of BaTi$_2$Sb$_2$O in Ref. [25], we find that we can satisfactorily explain the T_c trend with a spin-fluctuation pairing mechanism. We find that a sign-changing s-wave order parameter with nonuniform gap size on the various Fermi-surface sheets clearly dominates in Ba$_{1-x}$Na$_x$Ti$_2$Sb$_2$O at all doping levels. Explaining the nontrivial transition temperature trends of titanium based superconductors with isoelectronic doping and pressure are interesting future fields of study. Methodologically, it may be important to consider also the energy dependence within the FLEX.

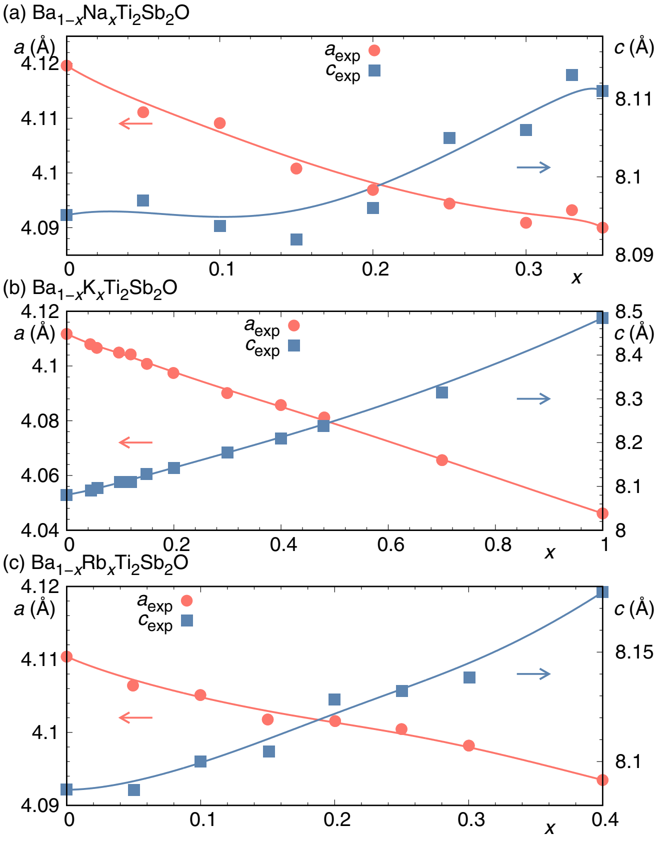

FIG. 7. Interpolation of experimental lattice constants.

ACKNOWLEDGMENTS

We acknowledge fruitful discussions with Y. Kubozono. Part of the computations were carried out at the Supercomputer Center at the Institute for Solid State Physics, the University of Tokyo. This work was supported by MEXT Leading Initiative for Excellent Young Researchers.

APPENDIX A: CRYSTAL STRUCTURES

We use experimental lattice parameters for $\mathrm{Ba}_{1-x}\mathrm{Na}_x\mathrm{Ti}_2\mathrm{Sb}_2\mathrm{O}$ from Ref. [9], for $\mathrm{Ba}_{1-x}\mathrm{K}_x\mathrm{Ti}_2\mathrm{Sb}_2\mathrm{O}$ from Ref. [14], and for $\mathrm{Ba}_{1-x}\mathrm{Rb}_x\mathrm{Ti}_2\mathrm{Sb}_2\mathrm{O}$ from Ref. [15]. They are shown as symbols in Fig. 7. We smoothly interpolate the lattice parameters in order to sample the doped crystal structures at regular intervals. Note that in the case of the c-lattice parameter of $\mathrm{Ba}_{1-x}\mathrm{Na}_x\mathrm{Ti}_2\mathrm{Sb}_2\mathrm{O}$ where the experimental lattice constants are rather nonmonotonous, the overall scale of the variation is small; as there is little justification for a dramatic doping dependence, we expect that the slight smoothing due to the interpolation is reducing errors rather than losing detail. The antimony positions are the only free positions in the $P4/mmm$ crystal structures, and we obtain them by relaxation using the FPLO basis [30] and the GGA exchange-correlation functional. Note that for the experimentally known $\mathrm{BaTi}_2\mathrm{Sb}_2\mathrm{O}$ structure the deviation in the Ti-Sb distance and the Sb-Ti-Sb angle is only 0.2% for the relaxed structure; this gives us confidence that the relaxation is reliable also for the doping series for which no experimental Sb position is available, in contrast to the well-known difficulties of the DFT structure prediction for iron-based superconductors [42]. We model the alkali-doping

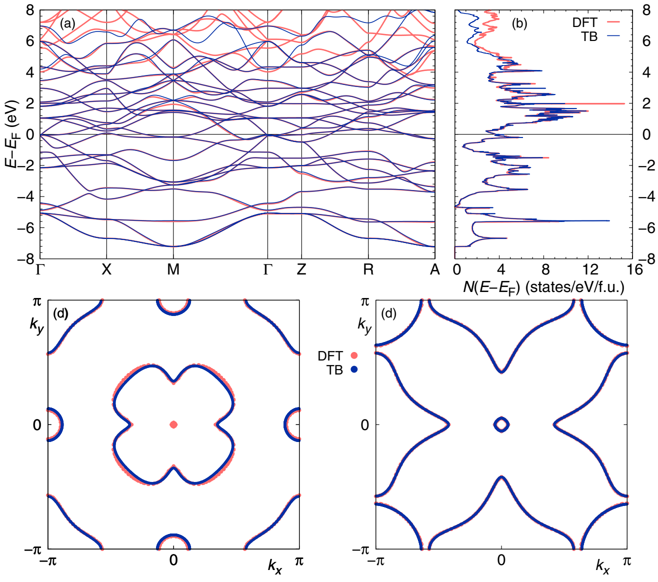

FIG. 8. Comparison between the density functional theory and the tight-binding model for $\mathrm{BaTi}_2\mathrm{Sb}_2\mathrm{O}$. (a) Band structure, (b) density of states, (c) Fermi surface at $k_z = 0$, and (d) Fermi surface at $k_z = \pi$. The agreement is excellent.

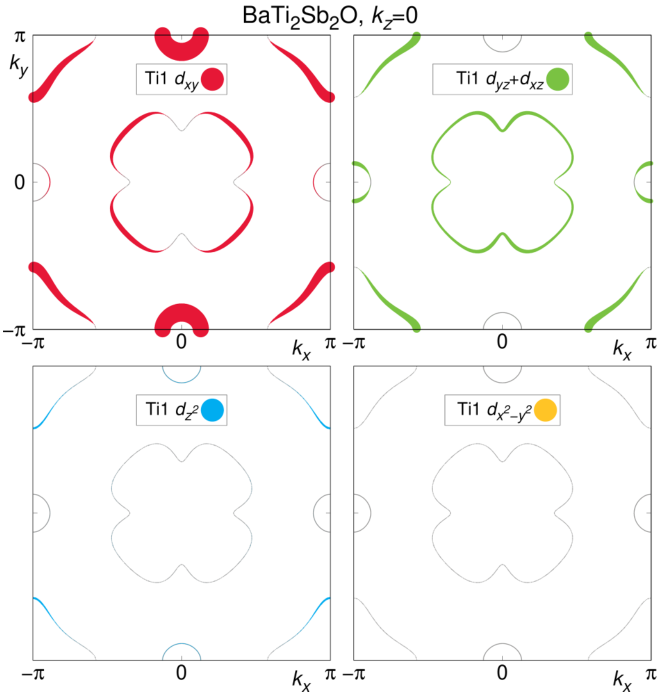

FIG. 9. Two-dimensional Fermi surface of $\mathrm{BaTi}_2\mathrm{Sb}_2\mathrm{O}$ with Ti $3d$ orbital character. All weights are shown with the same scale. The $3d_{xy}$ character clearly dominates, followed in importance by $3d_{yz}/3d_{xz}$. The $3d_{z^2}$ character is very faint, and the $3d_{x^2-y^2}$ character is negligible. Weights of the second Ti site are 90° rotated with respect to the first so that the sum has the C_4 symmetry of the space group.

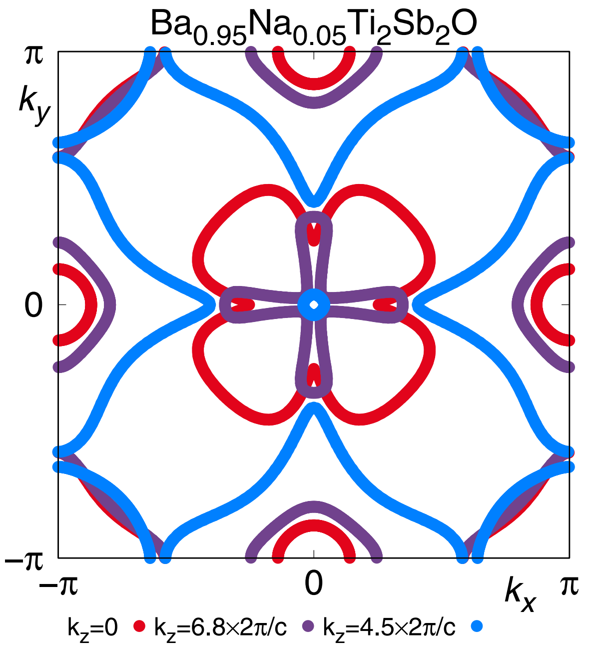

FIG. 10. Fermi surface of $Ba_{0.95}Na_{0.05}Ti_2Sb_2O$ at $k_z = 0$, $k_z = 0.5\pi$, and $k_z = \pi$, calculated within the GGA.

x by using the virtual crystal approximation for Ba using a nuclear charge between $Z = 55$ and 56.

APPENDIX B: TIGHT-BINDING MODEL

We use projective Wannier functions as implemented in FPLO [32] to construct faithful tight-binding models t_{ij}^{sp} of $BaTi_2Sb_2O$ and the alkali-doping series,

$$H_0 = -\sum_{i,j} t_{ij}^{sp} c^\dagger_{is\sigma} c_{jp\sigma}, \tag{B1}$$

where the t_{ij}s are transfer integrals between sites i and j, s and p are orbital indices, and σ is the spin. Figure 8 shows the quality of fit for band structure, density of states, and Fermi surface of $BaTi_2Sb_2O$; the agreement is nearly perfect. To achieve this, we need to include 26 orbitals: Ten Ti $3d$ orbitals, two Ti $4s$ orbitals, six Sb $5p$ orbitals, five Ba $5d$ orbitals, and three O $2p$ orbitals.

APPENDIX C: ELECTRONIC STRUCTURE

Figure 9 shows the weight of all $3d$ orbitals of Ti1 for $BaTi_2Sb_2O$. The Ti2 $3d$ orbitals have weights which are 90° rotated with respect to Ti1 (not shown). The dominating orbital is Ti $3d_{xy}$, and $3d_{xz}$, $3d_{yz}$ orbitals have some weight at the Fermi level as well. The $3d_{z^2}$ and $3d_{x^2-y^2}$ orbital contributions are negligibly small.

Figure 10 shows the Fermi surface of $Ba_{1-x}Na_xTi_2Sb_2O$ at $x = 0.05$ and compares favorably with the ARPES experiment of Ref. [40].

APPENDIX D: SPIN-FLUCTUATION FORMALISM

We consider the multiorbital Hubbard Hamiltonian [43],

$$H = H_0 + U\sum_{i,l} n_{il\uparrow} n_{il\downarrow} + \frac{U'}{2}\sum_{i,s,p\neq s} n_{is} n_{ip} - \frac{J}{2}\sum_{i,s,p\neq s} \boldsymbol{S}_{is}\cdot\boldsymbol{S}_{ip} + \frac{J'}{2}\sum_{i,s,p\neq s,\sigma} c^\dagger_{is\sigma} c^\dagger_{is\bar\sigma} c_{ip\bar\sigma} c_{ip\sigma}, \tag{D1}$$

with fermionic creation (annihilation) operators $c^\dagger_{is\sigma}$ ($c_{is\sigma}$), spin operator $\boldsymbol{S}_{is}$, density operator $n_{is\sigma} = c^\dagger_{is\sigma} c_{is\sigma}$, and interaction parameters U, U', J, and J' (the intraorbital Coulomb repulsion, the interorbital Coulomb repulsion, the Hund's rule coupling, and the pair-hopping term). The tight-binding part H_0 is given by Eq. (B1). Diagonalization of H_0 provides band energies $E_l(\boldsymbol{k})$ and matrix elements a_m^s and allows calculation of the static noninteracting susceptibility,

$$\chi_{st}^{pq}(\boldsymbol{q}) = -\sum_{\boldsymbol{k},l,m} a_l^{p*}(\boldsymbol{k}) a_l^t(\boldsymbol{k}) a_m^{s*}(\boldsymbol{k}+\boldsymbol{q}) a_m^q(\boldsymbol{k}+\boldsymbol{q}) \times \frac{n_F[E_l(\boldsymbol{k})] - n_F[E_m(\boldsymbol{k}+\boldsymbol{q})]}{E_l(\boldsymbol{k}) - E_m(\boldsymbol{k}+\boldsymbol{q})}, \tag{D2}$$

$n_F(E)$ is the Fermi distribution function. The observable static susceptibility can be calculated as

$$\chi_0(\boldsymbol{q}) = \frac{1}{2}\sum_{ab} \chi_{aa}^{bb}(\boldsymbol{q}). \tag{D3}$$

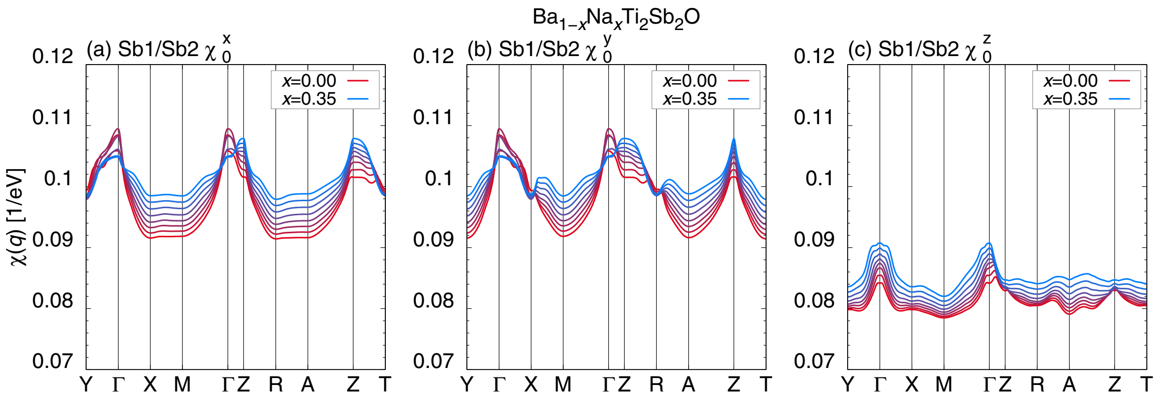

FIG. 11. Sb contribution to the noninteracting susceptibility χ_0 for $Ba_{1-x}Na_xTi_2Sb_2O$ along a $\mathbf{q}$ path. See Fig. 4 for the meaning of the path labels.

Applying the RPA, the charge and spin susceptibilities are calculated from the noninteracting susceptibility as

$$\begin{aligned} \left[\left(\chi_{\rm c}^{RPA}\right)^{pq}_{st}\right]^{-1} &= \left[\chi^{pq}_{st}\right]^{-1} + (U_{\rm c})^{pq}_{st}, \\ \left[\left(\chi_{\rm s}^{RPA}\right)^{pq}_{st}\right]^{-1} &= \left[\chi^{pq}_{st}\right]^{-1} - (U_{\rm s})^{pq}_{st}, \end{aligned} \tag{D4}$$

where nonzero components of the multiorbital Hubbard model interaction tensors are [43]

$$\begin{aligned} &(U_{\rm c})^{aa}_{aa} = U, \quad (U_{\rm c})^{aa}_{bb} = 2U', \\ &(U_{\rm c})^{ab}_{ab} = \tfrac{3}{4}J - U', \quad (U_{\rm c})^{ba}_{ab} = J' \\ &(U_{\rm s})^{aa}_{aa} = U, \quad (U_{\rm s})^{aa}_{bb} = \tfrac{1}{2}J, \\ &(U_{\rm s})^{ab}_{ab} = \tfrac{1}{4}J + U', \quad (U_{\rm s})^{ba}_{ab} = J'. \end{aligned} \tag{D5}$$

Then, the superconducting pairing vertex in the singlet channel is

$$\begin{aligned} \Gamma^{pq}_{st}(\mathbf{k},\mathbf{k}') = \Big[&\tfrac{3}{2}U_s\chi_s^{RPA}(\mathbf{k}-\mathbf{k}')U_s + \tfrac{1}{2}U_s \\ &- \tfrac{1}{2}U_c\chi_c^{RPA}(\mathbf{k}-\mathbf{k}')U_c + \tfrac{1}{2}U_c\Big]^{tq}_{ps}. \end{aligned} \tag{D6}$$

This vertex in orbital space is projected onto band space using the eigenvectors of H_0,

$$\begin{aligned} \Gamma_{ij}(\mathbf{k},\mathbf{k}') = &\sum_{s,t,p,q} a_i^{t*}(-\mathbf{k})a_i^{s*}(\mathbf{k}) \\ &\times \mathrm{Re}\big[\Gamma^{pq}_{st}(\mathbf{k},\mathbf{k}')\big]a_j^p(\mathbf{k}')a_j^q(-\mathbf{k}'), \end{aligned} \tag{D7}$$

and the gap equation,

$$\begin{aligned} &-\sum_j \oint_{C_j} \frac{dk'_\parallel}{2\pi}\frac{1}{4\pi v_F(\mathbf{k}')}[\Gamma_{ij}(\mathbf{k},\mathbf{k}') + \Gamma_{ij}(\mathbf{k},-\mathbf{k}')]g_j(\mathbf{k}') \\ &= \lambda_i g_i(\mathbf{k}) \end{aligned} \tag{D8}$$

is solved for the pairing eigenvalue λ_i and the gap function $g_i(\mathbf{k})$.

APPENDIX E: SUSCEPTIBILITY

The evolution of the Sb $5p_x$, $5p_y$, and $5p_z$ contributions to the noninteracting susceptibility of $Ba_{1-x}Na_xTi_2Sb_2O$ with doping level x is shown in Fig. 11. The values of the susceptibilities compared to Ti $3d$ orbitals are small (see the scale of Fig. 4), and their variation with the $\mathbf{q}$ value is tiny. With doping, the three susceptibilities grow even more featureless.

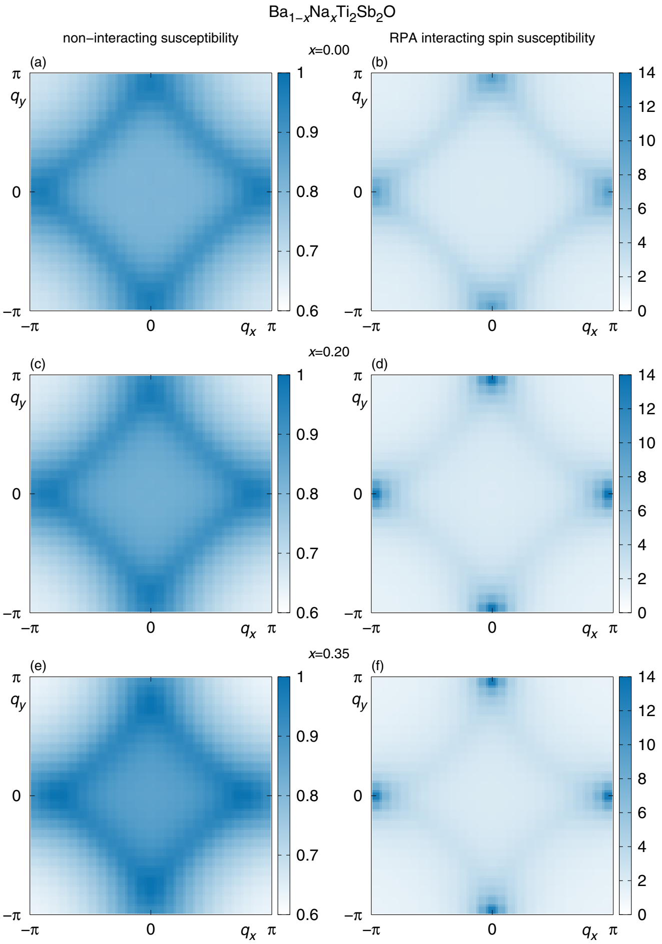

FIG. 12. Noninteracting susceptibility χ_0 and RPA interacting spin susceptibility χ_s for $Ba_{1-x}Na_xTi_2Sb_2O$.

The noninteracting susceptibility χ_0 and and RPA interacting spin susceptibility χ_s is shown in Fig. 12. This is based on a 3D calculation of χ_0 on a $25 \times 25 \times 9$ grid using a $25 \times 25 \times 9$ integration grid. The $q_z = 0$ cut shown in Fig. 12 is extracted using a 100×100 interpolation grid. The same interpolation grid was used for the interacting susceptibility χ_s shown in the main text, Fig. 5(a).

---

[1] A. Adam and H.-U. Schuster, Darstellung und kristallstruktur der pnictidoxide $Na_2Ti_2As_2O$ und $Na_2Ti_2Sb_2O$, Z. Anorg. Allg. Chem. **584**, 150 (1990).

[2] E. Axtell, T. Ozawa, S. M. Kauzlarich, and R. R. Singh, Phase transition and spin-gap behavior in a layered tetragonal pnictide oxide, J. Solid State Chem. **134**, 423 (1997).

[3] W. E. Pickett, Electronic instability in inverse-K_2NiF_4-structure $Na_2Sb_2Ti_2O$, Phys. Rev. B **58**, 4335 (1998).

[4] T. Yajima, K. Nakano, F. Takeiri, T. Ono, Y. Hosokoshi, Y. Matsushita, J. Hester, Y. Kobayashi, and H. Kageyama, Superconductivity in $BaTi_2Sb_2O$ with a d^1 square lattice, J. Phys. Soc. Jpn. **81**, 103706 (2012).

[5] T. Yajima, K. Nakano, F. Takeiri, J. Hester, T. Yamamoto, Y. Kobayashi, N. Tsuji, J. Kim, A. Fujiwara, and H. Kageyama, Synthesis and physical properties of the new oxybismuthides $BaTi_2Bi_2O$ and $(SrF)_2Ti_2Bi_2O$ with a d^1 square net, J. Phys. Soc. Jpn. **82**, 013703 (2013).

[6] T. Yajima, K. Nakano, F. Takeiri, Y. Nozaki, Y. Kobayashi, and H. Kageyama, Two superconducting phases in the isovalent solid solutions $BaTi_2Pn_2O$ (Pn = As, Sb, and Bi), J. Phys. Soc. Jpn. **82**, 033705 (2013).

[7] H.-F. Zhai, W.-H. Jiao, Y.-L. Sun, J.-K. Bao, H. Jiang, X.-J. Yang, Z.-T. Tang, Q. Tao, X.-F. Xu, Y.-K. Li, C. Cao, J.-H. Dai, Z.-A. Xu, and G.-H. Cao, Superconductivity,

charge- or spin-density wave, and metal-nonmetal transition in $BaTi_2(Sb_{1-x}Bi_x)_2O$, Phys. Rev. B **87**, 100502(R) (2013).

[8] X. F. Wang, Y. J. Yan, J. J. Ying, Q. J. Li, M. Zhang, N. Xu, and X. H. Chen, Structure and physical properties for a new layered pnictide-oxide: $BaTi_2As_2O$, J. Phys.: Condens. Matter **22**, 075702 (2010).

[9] P. Doan, M. Gooch, Z. Tang, B. Lorenz, A. Möller, J. Tapp, P. C. W. Chu, and A. M. Guloy, $Ba_{1-x}Na_xTi_2Sb_2O$ $(0.0 \leqslant x \leqslant 0.33)$: A layered titanium-based pnictide oxide superconductor, J. Am. Chem. Soc. **134**, 16520 (2012).

[10] R. H. Liu, D. Tan, Y. A. Song, Q. J. Li, Y. J. Yan, J. J. Ying, Y. L. Xie, X. F. Wang, and X. H. Chen, Physical properties of the layered pnictide oxides $Na_2Ti_2P_2O$ (P=As, Sb), Phys. Rev. B **80**, 144516 (2009).

[11] S. Kitagawa, K. Ishida, K. Nakano, T. Yajima, and H. Kageyama, s-wave superconductivity in superconducting $BaTi_2Sb_2O$ revealed by $^{121/123}$Sb-NMR/nuclear quadrupole resonance measurements, Phys. Rev. B **87**, 060510(R) (2013).

[12] F. von Rohr, A. Schilling, R. Nesper, C. Baines, and M. Bendele, Conventional superconductivity and charge-density-wave ordering in $Ba_{1-x}Na_xTi_2Sb_2O$, Phys. Rev. B **88**, 140501(R) (2013).

[13] Y. Nozaki, K. Nakano, T. Yajima, H. Kageyama, B. Frandsen, L. Liu, S. Cheung, T. Goko, Y. J. Uemura, T. S. J. Munsie, T. Medina, G. M. Luke, J. Munevar, D. Nishio-Hamane, and C. M. Brown, Muon spin relaxation and electron/neutron diffraction studies of $BaTi_2(As_{1-x}Sb_x)_2O$: Absence of static magnetism and superlattice reflections, Phys. Rev. B **88**, 214506 (2013).

[14] U. Pachmayr and D. Johrendt, Superconductivity in $Ba_{1-x}K_xTi_2Sb_2O$ $(0 \leqslant x \leqslant 1)$ controlled by the layer charge, Solid State Sci. **28**, 31 (2014).

[15] F. von Rohr, R. Nesper, and A. Schilling, Superconductivity in rubidium-substituted $Ba_{1-x}Rb_xTi_2Sb_2O$, Phys. Rev. B **89**, 094505 (2014).

[16] Y. Wang, X. Yang, T. Taguchi, H. Li, T. He, H. Goto, R. Eguchi, T. Miyazaki, Y.-F. Liao, H. Ishii, and Y. Kubozono, Preparation and characterization of superconducting $Ba_{1-x}Cs_xTi_2Sb_2O$, and its pressure dependence of superconductivity, Jpn. J. Appl. Phys. **58**, 110603 (2019).

[17] W. Ishii, T. Yajima, and Z. Hiroi, Electronic phase diagram of the titanium oxypnictide superconductor $BaTi_2(Sb_{1-x}Bi_x)_2O$, J. Phys.: Conf. Ser. **969**, 012052 (2018).

[18] Y. Wang, H. Li, T. Taguchi, A. Suzuki, A. Miura, H. Goto, R. Eguchi, T. Miyazaki, Y.-F. Liao, H. Ishii, and Y. Kubozono, Superconducting behavior of $BaTi_2Bi_2O$ and its pressure dependence, Phys. Chem. Chem. Phys. **22**, 23315 (2020).

[19] B. Lorenz, A. M. Guloy, and P. C. W. Chu, Superconductivity in titanium-based pnictide oxide compounds, Int. J. Mod. Phys. B **28**, 1430011 (2014).

[20] M. Gooch, P. Doan, Z. Tang, B. Lorenz, A. M. Guloy, and P. C. W. Chu, Weak coupling BCS-like superconductivity in the pnictide oxide $Ba_{1-x}Na_xTi_2Sb_2O$ ($x = 0$ and 0.15), Phys. Rev. B **88**, 064510 (2013).

[21] S. Kamusella, P. Doan, T. Goltz, H. Luetkens, R. Sarkar, A. Guloy, and H.-H. Klauss, CDW order and unconventional s-wave superconductivity in $Ba_{1-x}Na_xTi_2Sb_2O$, J. Phys.: Conf. Ser. **551**, 012026 (2014).

[22] S. Kitagawa, K. Ishida, W. Ishii, T. Yajima, and Z. Hiroi, Nematic transition and highly two-dimensional superconductivity in $BaTi_2Bi_2O$ revealed by ^{209}Bi-nuclear magnetic resonance/nuclear quadrupole resonance measurements, Phys. Rev. B **98**, 220507(R) (2018).

[23] A. Subedi, Electron-phonon superconductivity and charge density wave instability in the layered titanium-based pnictide $BaTi_2Sb_2O$, Phys. Rev. B **87**, 054506 (2013).

[24] D. J. Singh, Electronic structure, disconnected Fermi surfaces and antiferromagnetism in the layered pnictide superconductor $Na_xBa_{1-x}Ti_2Sb_2O$, New J. Phys. **14**, 123003 (2012).

[25] G. Zhang, J. K. Glasbrenner, R. Flint, I. I. Mazin, and R. M. Fernandes, Double-stage nematic bond ordering above double stripe magnetism: Application to $BaTi_2Sb_2O$, Phys. Rev. B **95**, 174402 (2017).

[26] X.-L. Yu, D.-Y. Liu, Y.-M. Quan, T. Jia, H.-Q. Lin, and L.-J. Zou, A site-selective antiferromagnetic ground state in layered pnictide-oxide $BaTi_2As_2O$, J. Appl. Phys. **115**, 17A924 (2014).

[27] H. Kim, J. H. Shim, K. Kim, and B. I. Min, Charge density waves and the Coulomb correlation effects in $Na_2Ti_2P_2O$ (P=Sb, As), Phys. Rev. B **96**, 155142 (2017).

[28] G. Wang, H. Zhang, L. Zhang, and C. Liu, The electronic structure and magnetism of $BaTi_2Sb_2O$, J. Appl. Phys. **113**, 243904 (2013).

[29] X.-W. Yan and Z.-Y. Lu, Layered pnictide-oxide $Na_2Ti_2Pn_2O$ (Pn=As, Sb): a candidate for spin density waves, J. Phys.: Condens. Matter **25**, 365501 (2013).

[30] K. Koepernik and H. Eschrig, Full-potential nonorthogonal local-orbital minimum-basis band-structure scheme, Phys. Rev. B **59**, 1743 (1999).

[31] J. P. Perdew, K. Burke, and M. Ernzerhof, Generalized Gradient Approximation Made Simple, Phys. Rev. Lett. **77**, 3865 (1996).

[32] H. Eschrig and K. Koepernik, Tight-binding models for the iron-based superconductors, Phys. Rev. B **80**, 104503 (2009).

[33] D. Guterding, H. O. Jeschke, P. J. Hirschfeld, and R. Valentí, Unified picture of the doping dependence of superconducting transition temperatures in alkali metal/ammonia intercalated FeSe, Phys. Rev. B **91**, 041112(R) (2015).

[34] D. Guterding, Microscopic modelling of organic and iron-based superconductors, Ph.D. thesis, Goethe-Universität Frankfurt, Germany, 2017.

[35] M. Shimizu, N. Takemori, D. Guterding, and H. O. Jeschke, Two-Dome Superconductivity In FeS Induced By A Lifshitz Transition, Phys. Rev. Lett. **121**, 137001 (2018).

[36] M. Shimizu, N. Takemori, D. Guterding, and H. O. Jeschke, Importance of the Fermi surface and magnetic interactions for the superconducting dome in electron-doped FeSe intercalates, Phys. Rev. B **101**, 180511(R) (2020).

[37] H. Hosono, K. Tanabe, E. Takayama-Muromachi, H. Kageyama, S. Yamanaka, H. Kumakura, M. Nohara, H. Hiramatsu, and S. Fujitsu, Exploration of new superconductors and functional materials, and fabrication of superconducting tapes and wires of iron pnictides, Sci. Technol. Adv. Mater. **16**, 033503 (2015).

[38] H. Nakaoka, Y. Yamakawa, and H. Kontani, Theoretical prediction of nematic orbital-ordered state in the Ti oxypnictide superconductor $BaTi_2(As, Sb)_2O$, Phys. Rev. B **93**, 245122 (2016).

[39] D. W. Song, J. Li, D. Zhao, L. K. Ma, L. X. Zheng, S. J. Li, L. P. Nie, X. G. Luo, Z. P. Yin, T. Wu, and X. H. Chen, Revealing the hidden order in $BaTi_2As_2O$ via nuclear magnetic resonance, Phys. Rev. B **98**, 235142 (2018).

[40] N. R. Davies, R. D. Johnson, A. J. Princep, L. A. Gannon, J.-Z. Ma, T. Qian, P. Richard, H. Li, M. Shi, H. Nowell, P. J. Baker, Y. G. Shi, H. Ding, J. Luo, Y. F. Guo, and A. T. Boothroyd, Coupled commensurate charge density wave and lattice distortion in $Na_2Ti_2Pn_2O$ (Pn=As,Sb) determined by x-ray diffraction and angle-resolved photoemission spectroscopy, Phys. Rev. B **94**, 104515 (2016).

[41] Z. Huang, W. L. Liu, H. Y. Wang, Y. L. Su, Z. T. Liu, X. B. Shi, S. Y. Gao, Z. C. Jiang, Z. H. Liu, J. S. Liu, X. L. Lu, Y. C. Yang, J. X. Zhang, S. C. Huan, W. Xia, J. H. Wang, Y. S. Wu, X. Wang, N. Yu, Y. B. Huang, S. Qiao, J. Li, W. W. Zhao, Y. F. Guo, G. Li, and D. W. Shen, Dual topological superconducting states in the layered titanium-based oxypnictide superconductor $BaTi_2Sb_2O$, arXiv:2009.06805.

[42] I. I. Mazin, M. D. Johannes, L. Boeri, K. Koepernik, and D. J. Singh, Problems with reconciling density functional theory calculations with experiment in ferropnictides, Phys. Rev. B **78**, 085104 (2008).

[43] S. Graser, T. A. Maier, P. J. Hirschfeld, and D. J. Scalapino, Near-degeneracy of several pairing channels in multiorbital models for the fe pnictides, New J. Phys. **11**, 025016 (2009).